APPLIED PHYSICS

Chemical and physical origins of friction on surfaces with atomic steps

Zhe Chen[1]*, Arash Khajeh[2]*, Ashlie Martini[2]†, Seong H. Kim[1]†

Friction occurs through a complex set of processes that act together to resist relative motion. However, despite this complexity, friction is typically described using a simple phenomenological expression that relates normal and lateral forces via a coefficient, the friction coefficient. This one parameter encompasses multiple, sometimes competing, effects. To better understand the origins of friction, here, we study a chemically and topographically well-defined interface between silica and graphite with a single-layer graphene step edge. We identify the separate contributions of physical and chemical processes to friction and show that a single friction coefficient can be separated into two terms corresponding to these effects. The findings provide insight into the chemical and topographic origins of friction and suggest means of tuning surfaces by leveraging competing frictional processes.

INTRODUCTION

Friction occurs at the interface between any two solid surfaces that are in contact and moving at different speeds or directions. Friction corresponds to wasted energy and therefore determines the efficiency and useful lifetime of all moving systems, from biological to aeronautical. At the macroscale, friction force (F_f) is often linearly proportional to the applied load (L). The proportionality constant of this relationship is called a friction coefficient [or coefficient of friction (COF), typically given the symbol μ]; thus, it can be expressed as $F_f = \mu \times L$, which is the well-known Amonton's law (*1*). At the nanoscale, adhesive forces (F_a) become significant and an additional term is introduced, $F_f = \mu \times (L + F_a)$ (*2*). Although this expression is phenomenologically simple and has been found to hold valid in experiments for decades, the actual mechanisms determining the magnitude of the COF are very complicated. Friction has been proposed to have purely physical origins (*3*, *4*) and to be related to chemical processes in sliding interfaces (*5*, *6*). However, the interplay of these two effects that ultimately results in observed friction is still poorly understood because often friction is associated with surface wear. In this study, we used a chemically and topographically well-defined interface to identify the contributions of physical and chemical processes to friction without wear and thereby obtain fundamental insights into the origin of the frequently reported but poorly understood COF.

RESULTS

Figure 1 schematically depicts the model system used in this study, which consists of an atomic force microscopy (AFM) probe and a graphite surface with a single-layer graphene step edge. The basal plane of graphite provides a chemically inert and defect-free flat surface. Because the graphene sheet exposed at the top surface is commensurate with the underlying layer (i.e., all topmost atoms are in registry with the underlying atoms), it provides the topographically least corrugated surface for friction tests (*7*). The single-layer graphene step edge that can be found on the graphite surface provides a well-defined topographic corrugation with a height change of precisely 0.34 nm over a distance corresponding to one chemical bond length (*8*). The carbon atoms at the graphene step edge are terminated with hydroxyl (C—OH) and alkyl (C—H) groups (fig. S1). The AFM probe made of silicon is covered with a native oxide; thus, it is hereafter referred to as a silica tip. This same system is modeled using reactive molecular dynamics (MD) simulation of the apex of the silica tip and the topmost three layers of graphene in the graphite near the step edge (fig. S2). Thus, it allows both experimental and computational studies of the interfacial shear of a silica surface on both an atomically flat surface and a chemically and topographically well-defined feature at the step. Upon confirmation of agreement between the experimental and computational friction responses, the simulations provide insight into the atomic-level origins of the friction.

Figure 2 shows the lateral force and height profiles measured from the AFM tip sliding over the graphite basal plane and moving up and down the graphene step edge at an applied load of 36.7 nN in dry nitrogen. Both sides of the graphene step edges are the basal plane of the graphite crystal, where the friction force (half the difference between the trace and retrace lateral forces) is only 0.15 ± 0.03 nN on both the upper and lower terraces. If this friction force is divided by the sum of the adhesion force (9.4 ± 0.8 nN) and the applied load (36.7 nN), it corresponds to a COF of 0.003. This value is consistent with the superlubricity reported for other types of carbon surfaces (*9*–*12*). However, when the AFM tip climbs up the step from the lower terrace to the upper terrace, friction increases by 30 to 40 times (positive lateral force in the step-up direction), giving a COF of about 0.1. This value is close to COFs observed for boundary lubrications by organic molecules on various surfaces under elastic deformation regimes (*13*). In contrast, more complicated friction responses are observed when the AFM tip slides down from the upper terrace to the lower terrace. Note that when the sliding direction is reversed, friction corresponds to a negative lateral force. During the step-down, friction first increases (negative lateral force), then decreases (change to positive lateral force) during the topographic height change, then increases again, and finally reaches the basal plane value as the tip moves away from the step edge.

The changes in friction observed at the step edge (Fig. 2) cannot be explained by topography alone. If the topographic effect was dominant, then the trace and retrace hysteresis at the step edge

[1]Department of Chemical Engineering and Materials Research Institute, Pennsylvania State University, University Park, PA 16802, USA. [2]Department of Mechanical Engineering, University of California, Merced, Merced, CA 95343, USA.
*These authors contributed equally to this work.
†Corresponding author. Email: amartini@ucmerced.edu (A.M.); shkim@engr.psu.edu (S.H.K.)

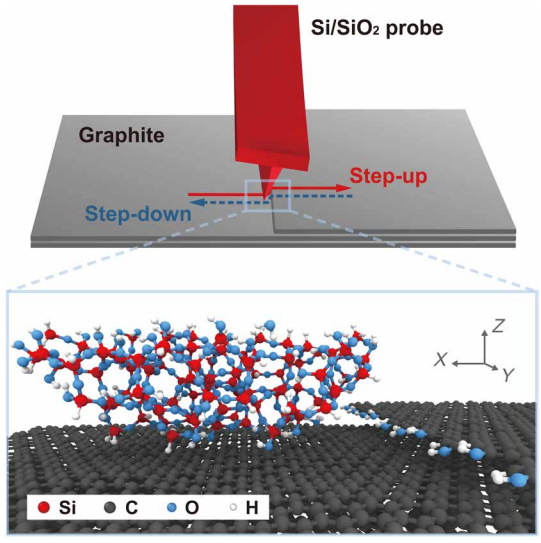

Fig. 1. Schematic illustration and atomic-scale rendering of a silica AFM tip sliding up and down a single-layer graphene step edge on an atomically flat graphite surface. The silica tip model represents the native oxide at the apex of the Si AFM tip used in the experimental study. This model system enables both experimental and computational studies that isolate the chemical and physical origins of friction.

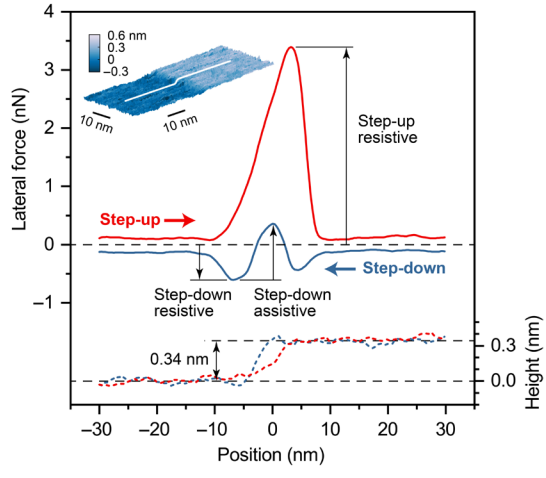

Fig. 2. Lateral force (solid lines) and height profile (dashed lines) measured at the graphene step edge with a silica AFM tip. The normal force applied to the tip was 36.7 nN, and the sliding speed was 500 nm/s. In the step-up direction, the positive lateral force means that the graphene step edge is resisting tip sliding. In the step-down direction, the negative lateral force is resistive to the tip sliding and the positive (or upward deviation from the negative trend) force is assistive to the tip sliding. The inset is the AFM topographic image of the graphene step edge obtained after repeated friction measurements at applied normal forces varying from 7.3 to 36.7 nN (fig. S3A); the postscan image shows no damage of the friction-tested region (white line). The height of the step edge is 0.34 nm, corresponding to the sum of the thickness of one graphene layer and the interlayer spacing between adjacent graphene layers.

should be the same as that on the basal plane and its center is shifted from the zero line (*14*). In the literature, the large friction (resistive force) during the step-down motion over various atomic steps has been explained in the context of a simple Prandtl-Tomlinson model with an additional potential barrier at the step edge called an Ehrlich-Schwoebel barrier (*15*, *16*). The concept of the Ehrlich-Schwoebel barrier was adapted from the diffusion barrier for atomic movements at a surface encountered in film growth studies (*17*). Although this phenomenological model can reproduce experimentally observed friction behavior, it does not provide molecular or atomistic insights into the origin of the Ehrlich-Schwoebel barrier. Previous modeling studies reproduced this barrier and demonstrated its ability to describe step edge friction, but the models did not explicitly include chemical reactions (*15*, *16*), so chemical and physical effects could not be differentiated. Here, to explore these origins, friction trends at the key points along the friction trace were analyzed as a function of load.

The trends shown in Fig. 2 were observed in AFM experiments performed at a range of loads (7.3 to 36.7 nN; fig. S3A) and sliding speeds (0.25 to 2 μm/s; fig. S3B), as well as reactive MD simulations performed at comparable pressures (fig. S4A). The experimentally observed trend is not a strong function of sliding speed (fig. S3C), and MD simulations performed at two sliding speeds exhibited the same trends (fig. S4B). The load dependence of friction on the graphite terrace and at the graphene step edge, from both experiment and simulation, is shown in Fig. 3. The qualitative trends from experiment and computation agree, despite differing size and time scale. This confirms that the simulations can provide atomistic insights into the interfacial processes responsible for complex friction behaviors at the single-layer graphene step edge as well as the superlubricity on the graphite basal plane.

The rate of change of friction with load at different positions along the friction trace is used to quantify COFs (Fig. 3), with the goal of isolating the chemical and physical contributions. The COF on the basal plane is in the superlubricity regime (*18*, *19*). However, during step-up, the COF increases by orders of magnitude. The step-down behavior is more complicated, as it consists of both assistive and resistive forces. The resistive force (positive friction) decreases slightly with load, corresponding to a small negative COF (*20*). Lastly, the assistive force (negative friction) during step-down becomes larger in magnitude with increasing load, corresponding to a moderate negative COF. All of these measurements of friction are for the same materials sliding under the same operating conditions. The fact that there are drastic differences in the COF, including a change in sign, depending on the relative position of the tip with respect to the step, demonstrates that these results could be used to identify different factors that contribute to friction. The atomic-scale information in the simulations is used to explore this.

Figure 4 shows the lateral force calculated from MD simulations at a load of 10 nN, along with the topographic height change (Fig. 4, A and B). The shear strain of the silica tip is used to quantify physical contributions to friction (Fig. 4, C and D), and chemical contributions are quantified by the number of hydrogen bonds formed between silica and graphite surface (Fig. 4, E and F). Gradual changes in the out-of-plane fluctuation amplitude of the carbon atoms on the upper and lower terraces (fig. S5) suggest that the tip sliding over the graphene step edge is a smooth process. When the silica tip is on the basal plane of graphite, there is no change in strain and no hydrogen bonding interaction across the interface. This is consistent with the expectation that the interlocking between atoms across the interface is negligible because the amorphous silica structure and the two-dimensional hexagonal array structure of graphite are incommensurate (*21*), there is no buckling of the

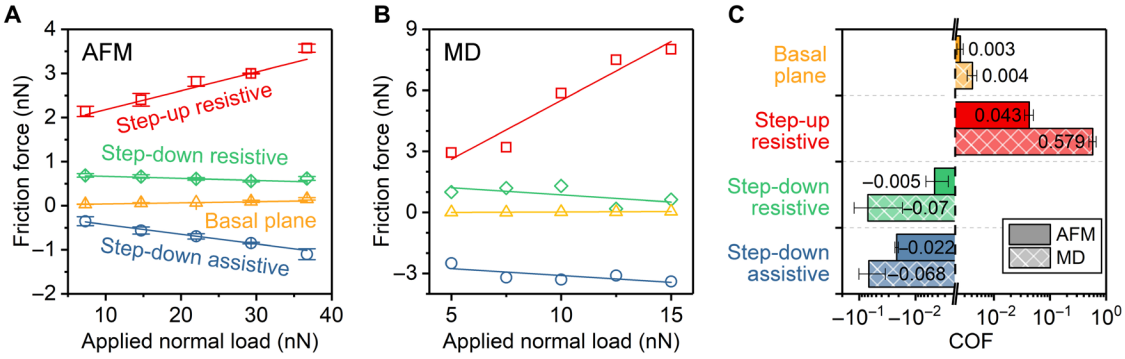

Fig. 3. Load dependence of friction force and corresponding COF. (**A**) Friction force measured with the silica AFM tip under various applied normal loads. The step-up resistive, step-down resistive, and step-down assistive forces are determined as marked in Fig. 2. The mean and SD were calculated from values of multiple measurements, where each measurement involved averaging over 128 scans. The SDs of the experimental values are similar to or smaller than the size of symbols. (**B**) Friction force calculated from reactive MD simulations. Note that, for the step-down case, a positive assistive lateral force corresponds to a negative friction force. (**C**) COF calculated from the load dependence of friction force, which is the slope of the least squares fitting lines in (A) and (B). The error bar in (C) indicates the uncertainty in the calculated slope. Because friction force for the cases of step-down resistive and step-down assistive decreases as the applied load increases, negative COF is obtained.

surface because the topmost graphene layer is in registry with the underlayer (*22*), and the basal plane of graphite is chemically inert (*23*, *24*). There are no significant physical or chemical interactions causing friction, which explains the superlubricity (COF of ~0.003) observed for the silica tip sliding on the graphite basal plane.

As the silica tip steps up over the graphene edge, the shear strain of the atoms in the tip increases in the direction opposite of the sliding motion (Fig. 4C). The degree of shear strain is the largest just before the center of mass of the tip moves to the upper terrace. In addition, the hydrogen bonding interactions between the silica tip and the C—OH groups at the graphene edge increase during the step-up (Fig. 4E), accompanied by the out-of-plane deformation of C—OH groups terminating the step edge (fig. S6). So, at step-up, the physical (strain) and chemical (hydrogen bonding) mechanisms synergistically enhance resistance to sliding, leading to a COF more than 100 times larger than that on the basal plane of graphite.

When the silica tip moves down the step from the upper terrace to the lower terrace, there is a small contribution from strain to assist sliding (the sign in Fig. 4D is opposite to the strain during step-up; Fig. 4C). However, hydrogen bonding between OH functional groups at the silica tip surface and the graphene step edge exerts a resistive force (Fig. 4F). This may also provide a physical explanation for the Ehrlich-Schwoebel barrier concept introduced previously to explain the resistive force at step-down. During sliding, physical and chemical mechanisms compete against each other; depending on their relative magnitudes, friction could be positive (resistive) or negative (assistive) as the tip moves down the step (fig. S3). The assistive effect due to shear strain is the largest when the center of mass of the tip transits from the upper terrace to the lower terrace, while the resistive effect due to hydrogen bonding interactions starts as soon as the leading edge of the tip approaches the graphene step edge and lasts until the trailing edge of the tip is separated from the graphene step edge. For this reason, the step-down resistive force due to hydrogen bonding interactions is observed over a large range around the step edge and the step-down assistive force from topography is seen only within the very narrow region near the step edge (Fig. 2).

DISCUSSION

Together, the observed COFs and analysis of the MD simulations provide insight into the physical and chemical origins of friction. Superlubricity is achieved when topography- and interlocking-induced strain and chemical bonding at the shear plane are negligible. The large friction during step-up over the 0.34-nm high graphene step edge can be attributed to synergy of physical effects due to topography and chemical effects due to interfacial bonding. During the step-down motion, the negative topography change produces a force assisting the sliding motion, whereas the chemical bonds between oppositely moving surfaces produce a resistive force. The balance of these two components will determine whether friction and the COF are positive or negative.

The topography effect can be explained in terms of the two forces acting on the AFM probe: the applied normal force from the cantilever and the force from the graphene step edge (fig. S7). The horizontal component of the force from the step edge contributes to the lateral force measured in the experiment. It is resistive for the step-up motion and assistive for the step-down motion, and its magnitude increases as the applied normal load increases. The chemical effect originates from interactions with the OH groups at the graphene step edge. This force always resists the motion, regardless of the scan direction, and its magnitude is related to the contact area between the tip and the surface (more accurately, the length over which the step edge crosses the contact area). According to the Derjaguin-Muller-Toporov (DMT) contact model (*25*), the contact area is proportional to the cube root of the normal force. Therefore, as the applied normal load increases, the assistive force due to the topographic height change increases much faster than the resistive force due to chemical interactions during the step-down motion, leading to a negative COF (*20*). When the topography-induced assistive force is larger than the chemistry-induced resistive force, negative friction can take place.

From Figs. 2 and 4 (A and B), it can be seen that chemical interactions at the step edge synergistically amplify the resistive force of topography while the tip ascends the step; in contrast, the cancelation effect between the resistive force due to chemical interactions and the assistive force from the topography effect during the descending motion is not as big as the amplification effect during the

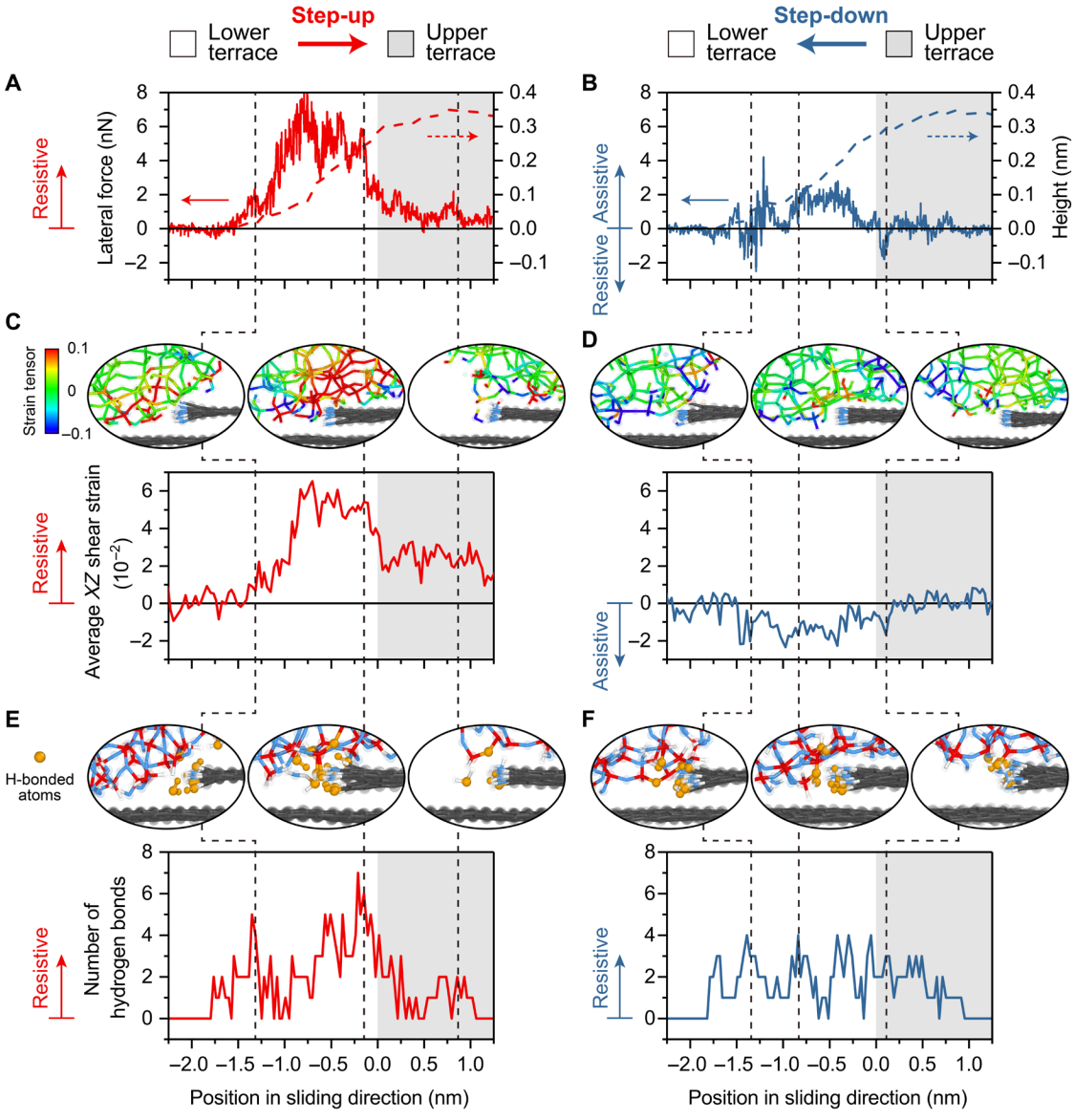

Fig. 4. Reactive MD simulation showing the origins of chemical and physical effects on friction. (**A** and **B**) Lateral force, (**C** and **D**) shear strain of atoms in the silica where the sign indicates direction relative to sliding, and (**E** and **F**) number of hydrogen bonds formed between the graphene step edge and the silica, calculated from simulations as a function of center-of-mass position of the tip with respect to the graphene step edge for (A, C, and E) step-up and (B, D, and F) step-down. The normal load applied to the silica tip is 10 nN, and the sliding speed is 10 m/s. The topographic height change measured with the center of mass of the counter surface is shown with dashed lines in (A) and (B) on the secondary *y* axis. The white and gray background areas are the lower and upper terraces, respectively. The snapshots of the shear strain of atoms in the silica and the hydrogen bonds bridging two surfaces at three locations for both step-up and step-down are also shown.

ascending motion. This may explain why achieving superlubricity is difficult on atomically rough surfaces unless the topographic surface features are chemically inert. As the atomic corrugation increases, friction increases due to both chemical (more site available for hydrogen bonding) and physical (larger topographical features) effects (fig. S8). When surface wear occurs during sliding, dangling bonds can be exposed at the worn surface as well as on wear debris and molecules impinging from the gas phase will react at those sites. In ambient air, reactive molecules are primarily oxygen and water, and their reactions lead to surface oxidation and hydroxylation. The findings of this study suggest that the oxygenated functional groups at the newly exposed topographically corrugated surfaces will greatly enhance interfacial friction when wear is involved.

The fact that physical and chemical factors can have opposite effects on friction of the surface with atomic-scale corrugations suggests that they might be leveraged to minimize sliding resistance at tribological interfaces. This concept is illustrated by the zero friction that is observed between the chemically and physically dominated regions during step-down (at lateral positions of −2.5 and 2.5 nm in Fig. 2). At these positions, friction is even smaller than the superlubricity observed on the basal plane. These findings suggest opportunities to tune the COF with prescribed topographic features and terminating species. While this concept may be impractical in an

industrial setting with current technology, fundamental understanding of chemical and topographic origins of friction holds great promise for future scientific advances and opens the possibility of tunable friction.

MATERIALS AND METHODS

Nanoscale friction measurement with AFM

A fresh graphite surface was generated by tape exfoliation of a ZYA-grade highly oriented pyrolytic graphite (HOPG) in ambient air. During the exfoliation, some graphene layers were inevitably torn, and new graphene edges were produced naturally. Thus, single-layer graphene step edges were easily found on the freshly exfoliated HOPG surface with AFM (MultiMode, Bruker), and nanoscale friction tests were performed in contact scan mode with a Si AFM probe (CONTV, Bruker; nominal spring constant: 0.2 N/m, nominal tip radius: 8 nm) in dry N_2 environment, as illustrated in Fig. 1. The N_2 came from a nitrogen generator. The dew point of the N_2 was typically around −35°C, which corresponds to the water concentration of 200 to 300 parts per million (ppm) at atmospheric pressure. The tip was covered with a native oxide layer. The tip was cleaned with ultraviolet (UV)/O_3 to remove organic contaminants (*26*); this process resulted in the silanol-terminated surface (Si—OH) (*27*). To confirm the Si—OH termination, water contact angle was measured on a model Si wafer before and after the same UV/ozone treatment (fig. S9). An excellent wettability with a water contact angle of ~0° confirmed that this cleaning method produces the clean surface fully terminated with hydroxyl groups (*28*, *29*). The normal spring constant of the cantilever was calibrated using Sader's method (*30*). The lateral sensitivity of the cantilever and detector was calculated by comparing the measured lateral signal (in units of millivolts) of a reference sample with a known friction force (in nanonewtons). The reference sample was a diamond-like carbon (DLC) coating, which gives a COF of ~0.15 in a pentanol vapor lubrication condition (at a partial pressure 40% of the saturation pressure) (*31*). During the friction test, the tip moved laterally in a reciprocating cycle in the direction perpendicular to the graphene step edge. The stroke length was 100 nm. Typically, a scan area containing only one graphene step edge was selected. The lateral force during the trace and retrace along the same line was recorded and averaged over 128 cycles at each condition. All friction tests were carried out at room temperature (22° to 25°C). The applied normal load varied in the range between 7.3 and 36.7 nN (with a force error at the step edge less than 0.02 nN; fig. S10), leading to an average contact pressure range of 1.6 to 2.8 GPa based on the Hertz contact model and 1.9 to 2.9 GPa based on the DMT contact model (*25*). The tip sliding speed ranged from 0.25 to 2 μm/s.

Characterization of HOPG surface

The newly generated HOPG surface was analyzed with polarization-modulation reflection-absorption infrared spectroscopy (PM-RAIRS). PM-RAIRS analysis was carried out with a Thermo Nicolet Nexus 670 spectrometer equipped with a custom-designed reflection-absorption unit consisting of a ZnSe polarization modulation crystal, an environment control cell, and a mercury cadmium telluride (MCT)-A detector (*32*). The PM operation was done using a photoelectric modulator (HINDS Instruments PEM-90) and a demodulator (GWC Instruments). The IR beam incidence angle was 81° from the surface normal. The PM-RAIRS spectra of the HOPG surface were normalized with the spectrum of clean gold obtained in dry Ar to remove the Bessel function shape background from the phase demodulation process.

MD simulations

To obtain molecular details at the atomic scale, the chemical and physical interactions between the atomically flat graphite surface with single-layer graphene step edge and the curved silica counter surface were modeled using MD simulation with a ReaxFF reactive force (*33*, *34*). All the simulations were done using the large-scale atomic/molecular massively parallel simulation (LAMMPS) software (*35*), and the postprocessing of results was carried out using the OVITO software (*36*).

The initial arrangement of the tip and the graphite is shown in fig. S2. The graphene step edge had an armchair structure (*37*). As suggested by the experimental measurements (fig. S1), the graphene edge in the simulation was terminated with hydroxyl groups and hydrogen atoms alternatively (*38*). To maintain the temperature at around 300 K, the NVT (fixed number of particles, volume, and temperature) ensemble with a Langevin thermostat was applied to all atoms that were not fixed or rigid.

Considering that there is a native oxide layer on the Si tip and only the apex of the tip is in contact with the graphite surface, the amorphous silica structure was used as a model tip in the simulation. The amorphous silica was produced by melting crystalline cristobalite at 4000 K and then by quenching to room temperature. To minimize the strain in the final amorphous structure, the heating and cooling rate was 0.02 K/fs, which was the slowest rate possible within the current computational constraints. Various properties of the amorphous silica model structure produced in this way were found to be comparable with experimentally measured properties (*39*). To reduce computational cost, the tip was constructed in a semicircular disc shape (fig. S2). The curvature (radius), thickness, and height of the disc were 2.5, 1.5, and 1.5 nm, respectively. To passivate the silica surface contacting the graphene surface, the undercoordinated silica and oxygen atoms were terminated with hydrogen atoms. The atoms in the top 0.5 nm of the tip were treated as a rigid body. To decrease the computational cost, only two mobile graphene layers were modeled at either side of the step edge.

Each MD simulation consisted of four steps: (i) energy minimization and equilibration of the tip and the substrate far from each other, (ii) downward movement of the tip at a speed of 10 m/s until the distance between the lowest atom in the tip was 0.2 nm from the top layer of the substrate, (iii) application of the normal load at the top rigid part of the tip and equilibration for 120 ps, and (iv) sliding of the tip at 10 m/s in the X direction by pulling using a harmonic spring with a stiffness of 6 N/m. MD simulations were performed for the step-up and step-down directions with loads of 5, 7.5, 10, 12.5, and 15 nN applied to the top rigid part of the tip. The real atomic area was calculated from the positions of atoms in the contact at each load (*40*), corresponding to a pressure between ~2.1 GPa at 5 nN and ~4.8 GPa at 15 nN. During the tip sliding process, the side boundaries of the graphite substrate were constrained to be fixed in all directions. The friction force during sliding was calculated from the sum of the X component of the forces on the atoms in the tip. Because of highly noisy force diagrams, a Fourier transform filtering was applied.

The shear strain of the silica tip along the sliding direction was quantified from the change in position of atoms relative to their neighboring atoms within a 0.5-nm cutoff distance. The cutoff radius

controls the number of neighbors that are included in the calculation of the deformation gradient tensor for each atom. This radius must be large enough to include at least three noncoplanar neighbors for every atom. The larger the cutoff, the larger the volume over which the local deformation gradient tensor is calculated (*41*, *42*). Here, the minimum cutoff radius (0.5 nm) was chosen to facilitate monitoring of the changes in the shear strain value.

The number of hydrogen bonds was calculated from the positions of donator oxygens, acceptor oxygens, and hydrogen atoms using the logic proposed by Guàrdia *et al.* (*43*). This calculation was performed for OH groups on the tip and an acceptor oxygen on the edge, and vice versa.

SUPPLEMENTARY MATERIALS

Supplementary material for this article is available at http://advances.sciencemag.org/cgi/content/full/5/8/eaaw0513/DC1

Supplementary Text
Fig. S1. PM-RAIRS spectra of graphite surface and Au surface.
Fig. S2. Front and side views of the MD simulation box.
Fig. S3. Lateral force of an AFM tip sliding across the graphene step edge.
Fig. S4. MD simulations of a tip sliding across a graphene step edge.
Fig. S5. Out-of-plane vibration of the carbon atoms on the upper and lower terraces.
Fig. S6. Out-of-plane deformation of C—OH groups terminating the graphene step edge.
Fig. S7. Force analysis diagram of the AFM tip at a graphene step edge.
Fig. S8. Lateral force of the AFM tip at multilayer graphene step edges.
Fig. S9. Water contact angle measurement on Si wafers.
Fig. S10. Applied normal force error in AFM experiments.
References (*44*–*47*)

REFERENCES AND NOTES

1. G. Amontons, De la résistance causée dans les machines. *Mem. Acad. R. A* **12**, 275–282 (1699).
2. B. Bhushan, J. N. Israelachvili, U. Landman, Nanotribology: Friction, wear and lubrication at the atomic scale. *Nature* **374**, 607–616 (1995).
3. F. P. Bowden, D. Tabor, *The Friction and Lubrication of Solids* (Oxford Univ. Press, 2001).
4. P. A. Thompson, M. O. Robbins, Origin of stick-slip motion in boundary lubrication. *Science* **250**, 792–794 (1990).
5. A. Noy, C. D. Frisbie, L. F. Rozsnyai, M. S. Wrighton, C. M. Lieber, Chemical force microscopy: Exploiting chemically-modified tips to quantify adhesion, friction, and functional group distributions in molecular assemblies. *J. Am. Chem. Soc.* **117**, 7943–7951 (1995).
6. K. Tian, N. N. Gosvami, D. L. Goldsby, Y. Liu, I. Szlufarska, R. W. Carpick, Load and time dependence of interfacial chemical bond-induced friction at the nanoscale. *Phys. Rev. Lett.* **118**, 076103 (2017).
7. A. K. Geim, Graphene: Status and prospects. *Science* **324**, 1530–1534 (2009).
8. J. S. Bunch, A. M. van der Zande, S. S. Verbridge, I. W. Frank, D. M. Tanenbaum, J. M. Parpia, H. G. Craighead, P. L. McEuen, Electromechanical resonators from graphene sheets. *Science* **315**, 490–493 (2007).
9. C. M. Mate, G. M. McClelland, R. Erlandsson, S. Chiang, Atomic-scale friction of a tungsten tip on a graphite surface. *Phys. Rev. Lett.* **59**, 1942–1945 (1987).
10. M. Dienwiebel, G. S. Verhoeven, N. Pradeep, J. W. M. Frenken, J. A. Heimberg, H. W. Zandbergen, Superlubricity of graphite. *Phys. Rev. Lett.* **92**, 126101 (2004).
11. A. Erdemir, Design criteria for superlubricity in carbon films and related microstructures. *Tribol. Int.* **37**, 577–583 (2004).
12. D. Berman, S. A. Deshmukh, S. K. R. S. Sankaranarayanan, A. Erdemir, A. V. Sumant, Macroscale superlubricity enabled by graphene nanoscroll formation. *Science* **348**, 1118–1122 (2015).
13. A. J. Barthel, S. H. Kim, Lubrication by physisorbed molecules in equilibrium with vapor at ambient condition: Effects of molecular structure and substrate chemistry. *Langmuir* **30**, 6469–6478 (2014).
14. D. F. Ogletree, R. W. Carpick, M. Salmeron, Calibration of frictional forces in atomic force microscopy. *Rev. Sci. Instrum.* **67**, 3298–3306 (1996).
15. H. Hölscher, D. Ebeling, U. D. Schwarz, Friction at atomic-scale surface steps: Experiment and theory. *Phys. Rev. Lett.* **101**, 246105 (2008).
16. P. Egberts, Z. Ye, X. Z. Liu, Y. Dong, A. Martini, R. W. Carpick, Environmental dependence of atomic-scale friction at graphite surface steps. *Phys. Rev. B* **88**, 035409 (2013).
17. R. L. Schwoebel, E. J. Shipsey, Step motion on crystal surfaces. *J. Appl. Phys.* **37**, 3682–3686 (1966).
18. H. Li, J. Wang, S. Gao, Q. Chen, L. Peng, K. Liu, X. Wei, Superlubricity between MoS_2 monolayers. *Adv. Mater.* **29**, 1701474 (2017).
19. Y. Song, D. Mandelli, O. Hod, M. Urbakh, M. Ma, Q. Zheng, Robust microscale superlubricity in graphite/hexagonal boron nitride layered heterojunctions. *Nat. Mater.* **17**, 894–899 (2018).
20. Z. Deng, A. Smolyanitsky, Q. Li, X.-Q. Feng, R. J. Cannara, Adhesion-dependent negative friction coefficient on chemically modified graphite at the nanoscale. *Nat. Mater.* **11**, 1032–1037 (2012).
21. M. Hirano, K. Shinjo, R. Kaneko, Y. Murata, Observation of superlubricity by scanning tunneling microscopy. *Phys. Rev. Lett.* **78**, 1448–1451 (1997).
22. C. Lee, Q. Li, W. Kalb, X.-Z. Liu, H. Berger, R. W. Carpick, J. Hone, Frictional characteristics of atomically thin sheets. *Science* **328**, 76–80 (2010).
23. H. Lee, H.-B.-R. Lee, S. Kwon, M. Salmeron, J. Y. Park, Internal and external atomic steps in graphite exhibit dramatically different physical and chemical properties. *ACS Nano* **9**, 3814–3819 (2015).
24. P. Blake, P. D. Brimicombe, R. R. Nair, T. J. Booth, D. Jiang, F. Schedin, L. A. Ponomarenko, S. V. Morozov, H. F. Gleeson, E. W. Hill, A. K. Geim, K. S. Novoselov, Graphene-based liquid crystal device. *Nano Lett.* **8**, 1704–1708 (2008).
25. B. V. Derjaguin, V. M. Muller, Y. P. Toporov, Effect of contact deformations on the adhesion of particles. *J. Colloid Interface Sci.* **53**, 314–326 (1975).
26. A. J. Barthel, J. Luo, K. S. Hwang, J.-Y. Lee, S. H. Kim, Boundary lubrication effect of organic residue left on surface after evaporation of organic cleaning solvent. *Wear* **350-351**, 21–26 (2016).
27. D. B. Asay, S. H. Kim, Evolution of the adsorbed water layer structure on silicon oxide at room temperature. *J. Phys. Chem. B* **109**, 16760–16763 (2005).
28. J. Rayss, A. Gorgol, W. Podkościelny, J. Widomski, M. Chołyk, Influence of the fused silica surface dehydroxylation on the adhesion of epoxyacrylate protective coatings used for optical fibers. *J. Adhes. Sci. Technol.* **12**, 293–303 (1998).
29. C. Chen, N. Zhang, W. Li, Y. Song, Water contact angle dependence with hydroxyl functional groups on silica surfaces under CO_2 sequestration conditions. *Environ. Sci. Technol.* **49**, 14680–14687 (2015).
30. J. E. Sader, I. Larson, P. Mulvaney, L. R. White, Method for the calibration of atomic force microscope cantilevers. *Rev. Sci. Instrum.* **66**, 3789–3798 (1995).
31. A. L. Barnette, D. B. Asay, M. J. Janik, S. H. Kim, Adsorption isotherm and orientation of alcohols on hydrophilic SiO_2 under ambient conditions. *J. Phys. Chem. C* **113**, 10632–10641 (2009).
32. I. Díez-Pérez, M. Luna, F. Teherán, D. F. Ogletree, F. Sanz, M. Salmeron, Interaction of water with self-assembled monolayers of alkylsilanes on mica. *Langmuir* **20**, 1284–1290 (2004).
33. T. P. Senftle, S. Hong, M. M. Islam, S. B. Kylasa, Y. Zheng, Y. K. Shin, C. Junkermeier, R. Engel-Herbert, M. J. Janik, H. M. Aktulga, T. Verstraelen, A. Grama, A. C. T. van Duin, The ReaxFF reactive force-field: Development, applications and future directions. *npj Comput. Mater.* **2**, 15011 (2016).
34. J. Yeon, A. C. T. van Duin, ReaxFF molecular dynamics simulations of hydroxylation kinetics for amorphous and nano-silica structure, and its relations with atomic strain energy. *J. Phys. Chem. C* **120**, 305–317 (2016).
35. S. Plimpton, Fast parallel algorithms for short-range molecular dynamics. *J. Comput. Phys.* **117**, 1–19 (1995).
36. A. Stukowski, Visualization and analysis of atomistic simulation data with ovito–the open visualization tool. *Modell. Simul. Mater. Sci. Eng.* **18**, 015012 (2010).
37. X. Jia, M. Hofmann, V. Meunier, B. G. Sumpter, J. Campos-Delgado, J. M. Romo-Herrera, H. Son, Y.-P. Hsieh, A. Reina, J. Kong, M. Terrones, M. S. Dresselhaus, Controlled formation of sharp zigzag and armchair edges in graphitic nanoribbons. *Science* **323**, 1701–1705 (2009).
38. G. Levita, P. Restuccia, M. C. Righi, Graphene and MoS_2 interacting with water: A comparison by ab initio calculations. *Carbon* **107**, 878–884 (2016).
39. A. Khajeh, X. He, J. Yeon, S. H. Kim, A. Martini, Mechanochemical association reaction of interfacial molecules driven by shear. *Langmuir* **34**, 5971–5977 (2018).
40. T. D. B. Jacobs, A. Martini, Measuring and understanding contact area at the nanoscale: A review. *Appl. Mech. Rev.* **69**, 060802 (2017).
41. M. L. Falk, J. S. Langer, Dynamics of viscoplastic deformation in amorphous solids. *Phys. Rev. E* **57**, 7192–7205 (1998).
42. F. Shimizu, S. Ogata, J. Li, Theory of shear banding in metallic glasses and molecular dynamics calculations. *Mater. Trans.* **48**, 2923–2927 (2007).
43. E. Guàrdia, J. Martí, L. García-Tarrés, D. Laria, A molecular dynamics simulation study of hydrogen bonding in aqueous ionic solutions. *J. Mol. Liq.* **117**, 63–67 (2005).
44. D. Tománek, W. Zhong, H. Thomas, Calculation of an atomically modulated friction force in atomic-force microscopy. *Europhys. Lett.* **15**, 887–892 (1991).
45. V. L. Popov, J. A. T. Gray, Prandtl-Tomlinson model: History and applications in friction, plasticity, and nanotechnologies. *J. Appl. Math. Mech.* **92**, 683–708 (2012).
46. G. Gao, R. J. Cannara, R. W. Carpick, J. A. Harrison, Atomic-scale friction on diamond: A comparison of different sliding directions on (001) and (111) surfaces using MD and AFM. *Langmuir* **23**, 5394–5405 (2007).

47. J. G. Vilhena, C. Pimentel, P. Pedraz, F. Luo, P. A. Serena, C. M. Pina, E. Gnecco, R. Pérez, Atomic-scale sliding friction on graphene in water. *ACS Nano* **10**, 4288–4293 (2016).

Acknowledgments
Funding: This work was supported by the NSF (grant nos. CMMI-1727356 and 1727571).
Author contributions: S.H.K. and A.M. conceived the idea and designed the experimental and computational works. Z.C. conducted AFM and IR experiments, and A.K. carried out MD simulations. Z.C., A.K., A.M., and S.H.K. interpreted the data and wrote the manuscript.
Competing interests: The authors declare that they have no competing interests. **Data and materials availability:** All data needed to evaluate the conclusions in the paper are present in the paper and/or the Supplementary Materials. Additional data related to this paper may be requested from the authors.

Submitted 13 November 2018
Accepted 27 June 2019
Published 9 August 2019
10.1126/sciadv.aaw0513

Citation: Z. Chen, A. Khajeh, A. Martini, S. H. Kim, Chemical and physical origins of friction on surfaces with atomic steps. *Sci. Adv.* **5**, eaaw0513 (2019).

Chemical and physical origins of friction on surfaces with atomic steps

Zhe Chen, Arash Khajeh, Ashlie Martini and Seong H. Kim

Sci Adv **5** (8), eaaw0513.
DOI: 10.1126/sciadv.aaw0513